bioRxiv preprint doi: https://doi.org/10.1101/2021.07.13.452147; this version posted July 13, 2021. The copyright holder for this preprint (which was not certified by peer review) is the author/funder. All rights reserved. No reuse allowed without permission.

Imaging and single cell sequencing analyses of super-enhancer activation mediated by NF-κB in B cells

Johannes N. Wibisana[1*], Takehiko Inaba[2,8], Hisaaki Shinohara[3,9], Noriko Yumoto[3], Tetsutaro Hayashi[4], Mana Umeda[4], Masashi Ebisawa[4], Itoshi Nikaido[4,5,6], Yasushi Sako[2], Mariko Okada[1,3,7,#]

[1]Laboratory for Cell Systems, Institute for Protein Research, Osaka University, Yamadaoka, Suita, Osaka 565-0871, Japan

[2]Cellular Informatics Laboratory, RIKEN, Wako, Saitama 351-0198, Japan

[3]RIKEN Center for Integrative Medical Sciences, Yokohama, Kanagawa 230-0045, Japan

[4]Laboratory for Bioinformatics Research, RIKEN Center for Biosystems Dynamics Research, Kobe, Hyogo 650-0047, Japan

[5]Functional Genome Informatics, Medical Research Institute, Tokyo Medical and Dental University, Bunkyo-ku, Tokyo 113-8510, Japan

[6]Master's/Doctoral Program in Life Science Innovation (Bioinformatics), Degree Programs in Systems and Information Engineering, Graduate School of Science and Technology, University of Tsukuba, Bunkyo-ku, Tokyo 113-8510, Japan

[7]Center for Drug Design and Research, National Institutes of Biomedical Innovation, Health and Nutrition, Ibaraki, Osaka, 567-0085, Japan

[8]Present address: Molecular Medicine and Cell Biology Laboratory, Division of Biological Science, Nara Institute of Science and Technology, Takayama-cho, Ikoma, Nara 630-0192, Japan

[9]Present address: Laboratory for Systems Immunology, Faculty of Pharmaceutical Sciences, Sanyo-Onoda City University, Daigakudori, Sanyo-onoda, Yamaguchi 756-0884, Japan

[#] Correspondence should be addressed to Mariko Okada; mokada@protein.osaka-u.ac.jp

bioRxiv preprint doi: https://doi.org/10.1101/2021.07.13.452147; this version posted July 13, 2021. The copyright holder for this preprint (which was not certified by peer review) is the author/funder. All rights reserved. No reuse allowed without permission.

Abstract

The NF-κB signaling pathway, which plays an important role in cell fate determination in various cells, has been found to be involved in the activation of long clusters of enhancers known as super-enhancers (SEs) for transcriptional regulation. However, the contribution of NF-κB to SEs has not yet been validated under microscopic observation. Using fluorescence imaging, single-cell transcriptome, and chromatin accessibility analyses, we show that NF-κB subunit RelA nuclear foci formation and single-cell gene expression demonstrate SE-like properties in anti-IgM-stimulated B cells. This contributed to bimodal and enhanced cell-to-cell variability in transcriptional response. Furthermore, we found that the predicted cis-regulatory interacting genomic regions from chromatin co-accessibility analysis were associated with the observed transcriptional heterogeneity. These findings suggest that NF-κB-mediated SE formation is important for the expression of NF-κB target genes and the amplification of transcriptional heterogeneity in response to environmental stimuli in B cells.

bioRxiv preprint doi: https://doi.org/10.1101/2021.07.13.452147; this version posted July 13, 2021. The copyright holder for this preprint (which was not certified by peer review) is the author/funder. All rights reserved. No reuse allowed without permission.

Introduction

The NF-κB signaling pathway, which plays important roles in cellular functions and cell fate determination[1–3], regulates B cells after B cell receptor (BCR) activation[4]. In BCR signaling, stimulation by antigens induces the canonical NF-κB pathway by activating protein kinase C β, kinase TAK1 (MAP3K7), BCL10, MALT1, and IκB kinase complex. This signaling cascade leads to the activation of IKKβ, which phosphorylates and promotes the proteasomal degradation of IκB. Since IκB masks the nuclear localization signal of NF-κB, its degradation promotes the nuclear translocation of p50 and RelA (p65) NF-κB heterodimer complex[5,6]. These then act as transcription factors, promoting the transcription of NF-κB target genes.

Anti-IgM has been reported to activate BCR and the NF-κB pathway, eliciting a dose-dependent all-or-none response in the nuclear translocation of NF-κB at the single-cell level[7] and causing cell-to-cell variability in transcriptional response[8]. This heterogeneity within the cell population may be responsible for the varying responses of B cells under the same environmental conditions in clonal selection[9,10]. Moreover, this heterogeneity in cell response upon NF-κB induction has also been observed in other cell types[11,12], indicating the presence of specific molecular functions associated with the transcriptional regulation of NF-κB. Furthermore, an earlier study found that the anti-IgM-induced all-or-none NF-κB nuclear translocation response was observed to lead to the formation of nuclear aggregates[7], hereby referred to as foci.

In this study, we hypothesized that these foci may be related to super-enhancer (SE)-mediated transcriptional regulation. SEs are long clusters of enhancers that have been reported to control cell identity and serve as nuclear platforms for the cooperative binding of transcription factors[13,14]. In previous chromatin immunoprecipitation sequencing (ChIP-seq) analyses using NF-κB and histone H3 lysine 27 acetylation (H3K27Ac) antibodies, NF-κB has been shown to be involved in SE activation along with other transcription factors[8,15] and coactivators, such as bromodomain protein 4 (BRD4)[16]. The aggregation of multiple transcriptional coactivators and mediators possessing intrinsically disordered regions (IDRs) promotes the formation of liquid-liquid phase separation (LLPS), which favors efficient gene transcription[17]. Together with mediator proteins and RNA polymerase II, these proteins have been observed under fluorescence microscopy[17,18] to form LLPS condensates at enhancer regions[19] through interaction of their activation domains[20]. However, the contribution of NF-κB to SEs has not yet been validated through microscopic observation.

We previously reported that anti-IgM dose-dependent NF-κB SE activity in primary B cells caused higher fold change and threshold gene expression, inducing a wider distribution of expression in the cell population[8]. This has also been observed in SE-regulated genes in embryonic stem cells[21]. In contrast, an earlier model of SE-mediated transcriptional regulation did not exhibit reductions in transcriptional noise[22]. Nevertheless, the behavior of NF-κB upon SE activation and its control over individual gene expression remain unclear. Therefore, we investigated the dynamics of NF-κB SE-mediated gene expression to confirm the function of the SEs.

bioRxiv preprint doi: https://doi.org/10.1101/2021.07.13.452147; this version posted July 13, 2021. The copyright holder for this preprint (which was not certified by peer review) is the author/funder. All rights reserved. No reuse allowed without permission.

The regulation of *NFKBIA* and *CD83*, which are known NF-κB target genes[23,24], were examined in this study. *NFKBIA* is an early response gene expressed upon NF-κB activation[25,26] that encodes IκBα, an NF-κB inhibitor. In contrast, *CD83* is a marker of B cell activation that is crucial for the development of B cells[27]. We used these two genes to represent NF-κB SE-mediated gene regulation since they are both regulated by NF-κB but have different biological functions.

In this study, we performed single-cell fluorescence imaging to assess the biochemical properties and dynamics of RelA foci upon anti-IgM stimulation in DT40 B cells. We then utilized scATAC-seq (single-cell assay for transposase accessible chromatin with sequencing) to investigate the changes in SE activity in B cells upon activation through chromatin accessibility and predict the cis-regulatory interactions of these regions through co-accessibility analysis[28]. We found that the formation of NF-κB nuclear aggregates upon nuclear translocation in anti-IgM-stimulated DT40 B cells exhibits switch-like dynamics with LLPS condensate-like biochemical properties. Single-cell sequencing analyses further showed that these SEs were related to the generation of enhanced transcriptional variation. These findings show that SEs are highly complex and that further study of SEs may elucidate the mechanism of SE-mediated gene regulation.

Results

RelA proteins form SE-like nuclear foci

We first observed under fluorescence imaging the RelA foci that formed in the nucleus upon nuclear translocation in DT40 cells of GFP-tagged RelA proteins, a component of the NF-κB heterodimer. We found that nuclear NF-κB maximally formed foci 20–30 min after anti-IgM stimulation (Fig. 1a, Supplementary Fig. 1a). As expected, an anti-IgM dose-dependent effect was observed in the numbers of RelA foci per cell, showing a bimodal distribution across doses (Supplementary Fig. 1b) that was observed in an earlier study[7]. Fitting the median number of foci of the dose-response curve to the Hill function resulted in a Hill coefficient of $N = 4.33$, suggesting that the formation of foci proceeded in a cooperative fashion (Fig. 1b). Since cooperative binding of transcription factors is a marker of SE-mediated gene regulation[17,29], our findings suggest that NF-κB localizes and activates the transcription of SE-dependent genes.

To further investigate the properties of the RelA foci, we focused on the relationship between NF-κB and BRD4. We generated DT40 cells co-expressing RelA-GFP and mKate2-BRD4S (see Methods section). These cells showed co-localization of BRD4S and NF-κB upon anti-IgM stimulation in a time-dependent manner (Fig. 1c–d). We further inhibited BRD4 activity by adding JQ1, a BET bromodomain inhibitor, 60 min before anti-IgM stimulation. The number of foci increased to a maximum point at 20 min, where the difference between the control and JQ1 treated cells was negligible, before significantly decreasing (Fig. 1e–f). In addition, JQ1 inhibition disrupted BRD4S puncta formation (Supplementary Fig. 2). This indicates that RelA foci formation itself is BRD4-independent, but foci maintenance is BRD4-dependent. This is consistent

bioRxiv preprint doi: https://doi.org/10.1101/2021.07.13.452147; this version posted July 13, 2021. The copyright holder for this preprint (which was not certified by peer review) is the author/funder. All rights reserved. No reuse allowed without permission.

with a previous report that found that BRD4 maintained active NF-κB through RelA binding[16]. On the other hand, inhibition of IκB kinase (IKK) using IKK-16 prevented the formation of RelA foci altogether (Fig. 1e–f), confirming that RelA foci formation is signal-dependent.

We next investigated the presence of LLPS-like properties in RelA foci. We used PONDR VLXT to analyze the IDRs and found that RelA had high disorder scores in 250–500 amino acid residues, which is comparable to BRD4 (Supplementary Fig. 3a)[30]. In addition, it was previously determined through experimental approaches that RelA possessed IDRs[31]. To examine whether the RelA foci exhibited LLPS condensate-like properties, we treated cells with 1,6-hexanediol (1,6-HD), a compound known to promote the dissolution of liquid-like condensates[32]. Fluorescence imaging analysis (Fig. 1g, Supplementary Fig. 3b) showed that treatment with 1,6-HD after 20 min of anti-IgM stimulation dramatically reduced the number of foci and that washing recovered the foci. These results suggest that the RelA foci were similarly regulated and were responsible for anti-IgM-dependent SE formation.

NF-κB-dependent SE-regulated genes demonstrated SE-like transcriptional dynamics

Next, we analyzed the transcriptional responses of anti-IgM stimulated single cell populations (n=453) at various anti-IgM doses (0, 0.1, 1, and 10 μg/mL; Supplementary Table 1) using RamDA-seq with an oligo-dT primer, a method for single-cell RNA sequencing[33]. Using Seurat, we obtained two distinct cell clusters (Fig. 2a)[34]. This suggests the presence of two discrete cell populations, such as those obtained in the imaging analysis. We classified these clusters as activated (red cluster) and inactivated (blue cluster), as determined by their mean expression levels of representative NF-κB target genes, such as *NFKBIA*, *CD83*, and *TNFAIP3*[35] (Fig. 2b).

Prediction of cell activation through logistic regression analysis on the number of foci per cell showed similar quantitative profiles in cell activation, in which most cells were activated at 1 and 10 μg/mL as well as inactivated at 0 and 0.01 μg/mL doses of anti-IgM (Fig. 2c, Supplementary Table 2). This suggests that the cell states determined from the scRNA-seq and imaging analysis were closely related.

Since the cells exhibited bimodal responses, we investigated how gene expression variability changed across different concentrations of anti-IgM stimulation. To investigate the heterogeneity of gene expression at each dose point, we calculated the Fano factor of 1337 differentially expressed genes (DEGs) that were upregulated in the activated cells compared with inactivated cells from the scRNA-seq analysis. The Fano factor (Ω^2/μ), which is typically used to calculate changes in transcriptional bursting[36,37], provides a measure of deviation from the Poisson distribution where $\Omega^2/\mu = 1$. Hierarchical clustering analysis across dose points yielded 4 modes of variability modulation: decreasing along dose points (cluster 1), increasing only at 0.1 μg/mL (cluster 2), increasing at 0.01 and 1 μg/mL (cluster 3), and increasing along dose points (cluster 4) (Fig. 2d). We focused on clusters 2 and 4. Cluster 2 showed low variability between low and high doses compared to the intermediate dose point (Fig. 2c), which is similar to the observed cell state (Fig. 1c). Additionally, this cluster

bioRxiv preprint doi: https://doi.org/10.1101/2021.07.13.452147; this version posted July 13, 2021. The copyright holder for this preprint (which was not certified by peer review) is the author/funder. All rights reserved. No reuse allowed without permission.

contained representative NF-κB negative modulators such as *NFKBIA*[2] and *TNFAIP3*[38]. The high variability of gene expression at intermediate anti-IgM concentrations (0.1 μg/mL) may be related to dose-dependent cell activation, in which steep changes in the frequency of RelA foci formation were observed (Supplementary Fig. 1b). Cluster 4 contains genes encoding immunoreceptors, such as *CD83,* and transcription factors, such as *FOSL2*, showing increasing variability across dose points. This result indicates that the expression of these genes is variable even when most cells are in the activation state. From these findings, we selected *NFKBIA* and *CD83* as representative genes for further analysis.

Since the cells exhibited two discrete states with increasing concentrations of anti-IgM stimulation (Fig. 2a), we performed a pseudo-time analysis to visualize the gene expression across cellular states leading to cell activation (Supplementary Fig. 4a). This was performed since some genes may be correlated with cellular states rather than anti-IgM concentration. For example, we found that *NFKBIA* exhibited bimodal expression at 0.1 μg/mL anti-IgM (Supplementary Fig. 4b). The pseudo-time analysis further showed that the two cell populations were discrete (Supplementary Fig. 4c). Additionally, *NFKBIA* and *CD83* showed different dynamics across pseudo-time. For *NFKBIA*, the inactivated cells demonstrated slightly higher gene expression than *CD83*, whereas cells at later activation stages demonstrated switch-like high gene expression. Moreover, *NFKBIA* exhibited bimodal expression across all cells. On the other hand, *CD83* had lower basal expressions across the inactivated cells but enhanced diverse expression levels at later cell activation stages (Fig. 2e). This indicates that the transcriptional regulation between these two genes upon cell activation was potentially controlled by different modes.

To validate the changes in transcriptional dynamics of the NF-κB-regulated genes upon anti-IgM stimulation from scRNA-seq, we quantified their cellular mRNA using smRNA-FISH (single-molecule RNA-FISH) (Fig. 2f–g). There was a positive correlation between the RelA foci number and mRNA expression of both genes at all dose points (Supplementary Fig. 5a–b). We also confirmed that the RelA foci numbers per cell across doses of the *CD83* and *NFKBIA* smRNA-FISH samples were similar (Supplementary Fig. 5c), suggesting that the technical differences between the samples were minimal. It should be noted that the correlation coefficient was lower at doses of 1 and 10 μg/mL since most cells were expected to be activated. However, the correlation at a dose of 0 μg/mL between *NFKBIA* mRNA and GFP was lower than that of *CD83* mRNA and GFP, which may be attributed to the high basal transcription of *NFKBIA* mRNA prior to cell activation (Fig. 2e). Moreover, the trend previously observed across dose points in scRNA-seq (Supplementary Fig. 4b) was also observed in the smRNA-FISH (Supplementary Fig. 5d).

As expected, we were able to reproduce the expression trend in RNA-seq data using smRNA-FISH (Fig. 2g, Supplementary Fig. 6). We then calculated the Fano factor change between cells at doses of 10 and 0 μg/mL, where the cells were predominantly activated and inactivated, respectively. We observed a significantly higher change in heterogeneity associated with *CD83* (RNA-seq: 2.7, RNA-FISH: 10.1) compared to *NFKBIA* (RNA-seq: 1.1, RNA-FISH: 1.7). Furthermore, stimulation with other anti-IgM concentrations demonstrated a high bimodality of *NFKBIA* expression across doses,

bioRxiv preprint doi: https://doi.org/10.1101/2021.07.13.452147; this version posted July 13, 2021. The copyright holder for this preprint (which was not certified by peer review) is the author/funder. All rights reserved. No reuse allowed without permission.

whereas expression of *CD83* demonstrated a long-tailed distribution (Supplementary Fig. 5d), which may be explained by its larger transcriptional burst size[39].

To clarify the underlying transcriptional mechanism, we performed epigenetic analysis on SEs and their effects on transcription. Traditionally, SE analysis is performed using transcription factors, histone acetylation ChIP-seq, or DNase-seq data[13,14,29]. In our research, we utilized ATAC-seq data to investigate a large stretch of enhancers similar to SEs since these have been reported to correlate with transcription factors and histone acetylation ChIP-seq signals in SEs[8]. In particular, we examined changes in chromatin accessibility before and after cell activation through anti-IgM stimulation.

Stitching of ATAC peaks was performed for peaks within 5 kb of each other, which is shorter than the default (12.5 kb) since ATAC peaks are often broader than transcription factor ChIP-seq peaks[40]. In addition, we aimed to resolve more closely packed enhancers by selecting a narrower peak stitching distance. The rank-ordering of super-enhancers (ROSE) algorithm was then implemented to rank the enhancers in the samples with and without anti-IgM stimulation (Fig. 3a)[13,41]. Changes in chromatin accessibility between the unstimulated and stimulated cells were acquired by obtaining the merged peaks and calculating the fold changes of the signals between both conditions (see Methods). We then classified the enhancers as gained, lost, or unchanged by the quantiles for TEs (typical enhancers) and SEs (Supplementary Fig. 7a). We found that both *CD83* and *NFKBIA* were present in the gained SE-associated genes (Fig. 3b); however, *NFKBIA* showed less accessibility differences upon stimulation (Fig. 3c). These results suggest that *CD83* was more highly influenced by SEs than *NFKBIA*.

RT-qPCR analysis revealed that *CD83* expression was sustained, while *NFKBIA* expression was transient (Fig. 3d), suggesting that the differences in transcriptional regulation between these genes may be related to their functions. Then, we treated cells with IKK-16 and JQ1 60 min before anti-IgM stimulation to investigate the dependences of *CD83* and *NFKBIA* on SEs. We confirmed that both genes were NF-κB-regulated since IKK-16 treatment suppressed the expression of both genes (Fig. 3e). In contrast, JQ1 treatment suppressed *CD83* expression significantly, while *NFKBIA* expression increased proportionally with higher JQ1 concentration (Fig. 3f), suggesting that *CD83* gene expression was more highly controlled by SE than *NFKBIA*.

We identified genes associated with changes in accessibility and transcriptional activity by comparing genes with gained SEs with the positively upregulated genes from RNA-seq analysis of the activated cell cluster. We identified 52 genes with gained SEs associated with upregulated RNA expression (Supplementary Fig. 7b). Gene Ontology analysis of these 52 genes revealed that a high proportion of these genes exhibited enriched functions related to immune cell activation and regulation (Supplementary Fig. 7c). These results confirm that SE-regulated genes play an important role in cellular decisions, such as in B cell development.

bioRxiv preprint doi: https://doi.org/10.1101/2021.07.13.452147; this version posted July 13, 2021. The copyright holder for this preprint (which was not certified by peer review) is the author/funder. All rights reserved. No reuse allowed without permission.

Predicted cis-regulatory interactions correlate with transcriptional heterogeneity

Due to the complex arrangement of high-order chromatin structures involving SE-mediated gene expression, it remains difficult to generalize the contribution of SEs to transcriptional regulation[42]. Therefore, we utilized single-cell ATAC-seq data for co-accessibility analysis using Cicero to elucidate the epigenetic regulation of *CD83* and *NFKBIA*[28]. In this analysis, we predicted accessible genomic regions that were potentially in close physical proximity by determining their co-accessibility scores and changes upon cell stimulation. Co-accessibility calculations were performed separately for the stimulated and unstimulated samples. The peaks used for co-accessibility analysis were obtained by merging shortly-stitched peaks (108 bp) from both samples. Regions were filtered based on co-accessibility scores ≥ 0.1 in the stimulated samples and ≥ 0.05 in differences between the stimulated and unstimulated samples.

We then examined upregulated genes in the activated cells that gained SEs or TEs upon stimulation to analyze the effects of chromatin accessibility and gene expression noise. We found that the ratio of Fano factor between anti-IgM doses 10 and 0 μg/mL were positively correlated (Fig. 4a), in which genes with gained SEs had higher correlations. To determine whether co-accessibility was correlated with gene expression amplitude and noise, we annotated each gene with co-accessible pairs above the threshold and observed a positive correlation between the number of regions with co-accessible pairs and their RNA fold changes (Fig. 4b) or Fano factor ratios (Fig. 4c). These results suggest that co-accessibility is a suitable predictor of gene expression levels or transcriptional variations.

To closely compare *CD83* and *NFKBIA*, we visualized the co-accessible region pairs within thresholds between peaks residing ±1 kb of each gene annotated transcriptional start site (TSS) as well as other positions in the same chromosome. Surprisingly, no co-accessible regions paired with the peaks ±1 kb of the *NFKBIA*-annotated TSS were observed. However, several regions associated with *CD83* were observed (Fig. 4d–e), indicating the formation of higher chromatin interactions upon cell activation. In total, we identified three regions (2 within SE and 1 outside SE) above our set threshold that did not intersect the gene bodies of other annotated genes (Fig. 4d–e).

Discussion

First, we characterized RelA foci through fluorescence imaging analysis, demonstrating the SE condensate-like properties, such as binding cooperativity, LLPS perturbation sensitivity, and BRD4 dependence. This showed that NF-κB-dependent SE nuclear aggregates also exhibited properties similar to those of known SE condensates[19,20,22,43].

SE-mediated gene regulation has been reported to cause transcriptional heterogeneity[21] and threshold gene expression[8]. However, another report showed that

bioRxiv preprint doi: https://doi.org/10.1101/2021.07.13.452147; this version posted July 13, 2021. The copyright holder for this preprint (which was not certified by peer review) is the author/funder. All rights reserved. No reuse allowed without permission.

transcriptional noise was reduced in SE-mediated gene regulation[22]. Through experimental and computational approaches, we showed that NF-κB-mediated SE formation strongly modulated transcriptional heterogeneity. This was observed in *CD83*, a B cell activation marker, demonstrating its involvement in cell fate determination in B cell development.

Our analysis also showed that sequence-based identification of SEs may not truly reflect the biological functions of SEs for each target gene. For example, *NFKBIA* and *CD83* mRNAs exhibited varying sensitivities to JQ1 (Fig. 3e). Since the *NFKBIA* SE had a constitutively open chromatin prior to anti-IgM stimulation (Fig. 3a), the signal-dependent effect on SE regulation of *NFKBIA* appeared to be small. The observed dynamics of *NFKBIA* in this study are also consistent with a previous report stating that bimodality of gene expression can be produced even in noncooperative systems[44]. The long-tailed mRNA distribution, as shown by *CD83*, has been reported to be crucial to the regulation of immune cell-mediated cytokine secretion[45] and inflammatory responses[46]. These two genes demonstrated large fold-changes in gene expression and transcriptional heterogeneity upon SE regulation. However, the molecular regulation of SE in each gene varied. Therefore, our results suggest that the functional evaluation of SE should not solely rely on sequence analysis, but also on other experimental methods.

We hypothesized that it is difficult to generalize transcriptional dynamics solely through genome-wide SE analysis since SEs refer to a broad group that consist of smaller regulatory elements with different properties contributing to gene expression regulation[47]. For example, different enhancer elements may have sub-additive and additive properties in the activation of gene expression in *Drosophila* development[48]. In the context of SE, it is still unclear how these singular elements, such as biochemical properties, cause external effects. Therefore, analysis of potential enhancer contacts may resolve this issue.

To confirm our findings, we utilized a CRISPR-Cas9 system with double-flanking gRNA to induce long deletion in regions with the highest co-accessibility scores in the *CD83* promoter (Fig. 4d–e). Unfortunately, we were unable to confirm the deletion of the regions within *CD83* SE, which may be attributable to the incomplete genome database of the reference genome used for the gRNA design (GRCg6a). We were able to induce a long deletion in the enhancer region outside of the *CD83* SE. However, the obtained cell clone demonstrated low survival and impaired proliferation rates. Thus, we were unable to confirm the changes in gene expression dynamics upon deletion of this enhancer region.

These results provide insight into the mechanism of SE-mediated gene regulation in the NF-κB pathway, and similar methods may be applied to further study other signaling pathways regulated by SEs.

Materials and methods

bioRxiv preprint doi: https://doi.org/10.1101/2021.07.13.452147; this version posted July 13, 2021. The copyright holder for this preprint (which was not certified by peer review) is the author/funder. All rights reserved. No reuse allowed without permission.

DT40 cell culture

Wild-type and RelA-GFP-expressing DT40 cells were obtained from Dr. Shinohara. The DT40 cells were cultured in RPMI-1640 without phenol red (Wako) supplemented with 10% fetal bovine serum (Sigma-Aldrich), 1% (v/v) chicken serum (Nippon Bio-test Laboratories), 75 μM 2-mercaptoethanol (Gibco), 1 mM sodium pyruvate (Wako, Japan), 1% (v/v) penicillin-streptomycin solution (Nacalai Tesque), 1% (v/v) 100x MEM non-essential amino acids solution (Wako), and 2 mM L-glutamine (Nacalai Tesque). The cells were cultured at 39°C and 5% CO_2 in a humidified incubator.

JQ1, IKK-16, and 1,6-hexanediol cell treatment

For JQ1 and IKK-16 inhibition, the DT40 cells were suspended in 5 μM JQ1 (Selleckchem) and 6 μM of IKK-16 (Selleckchem) 60 min before anti-IgM stimulation. For 1,6-hexanediol inhibition, 5% of 1,6-hexanediol (Sigma-Aldrich) was added after anti-IgM stimulation.

Quantification of RelA foci in single cells

An inverted microscope IX81 (Olympus) equipped with a CSU-X1 confocal scanner unit (Yokogawa) and oil-immersion objective (100x, NA 1.45) was used to obtain images. MetaMorph software (Molecular Devices) was used to obtain 13 z-slices of stack images at 1 μm increments in the z-direction. The image resolution used was 512 × 512 pixels (1 pixel = 0.16 μm). The observation chamber was maintained at 39°C during observation. FIJI ImageJ 1.52i (https://imagej.net/Fiji/Downloads) was used to count the foci using a custom macro, where the diameter for foci detection was set to 0.96 μm.

Quantification using smRNA-FISH

Fluorescence-conjugated chicken *GAPDH*, *CD83*, and *NFKBIA* probes were generated for smRNA-FISH using the Stellaris Probe Designer (https://www.biosearchtech.com/support/tools/design-software/stellaris-probe-designer) according to the protocols of Biosearch Technologies. A total of 1×10^7 DT40 cells in 600 μL RPMI without supplements were stimulated with anti-IgM or PBS (control) for 30 min before washing with PBS and resuspending in 1 mL suspension buffer. Procedures following cell fixation were performed as described in the manuals of Biosearch Technologies for suspension cells. The fixed cells were mounted using Vectashield (Vector Laboratories), sandwiched in cover glasses (Matsunami Glass), and sealed with clear nail polish prior to imaging.

A DeltaVision Elite - Olympus IX71 (Olympus) fluorescence microscope equipped with a Photometrics Coolsnap HQ2 camera and an oil-immersion objective (60x, NA 1.42) was used for image acquisition. SoftWoRx software (Applied Precision) was used for image acquisition and deconvolution. FISH-quant v3 was used to quantify the RNA-FISH images[49]. The default parameters were used in the quantification.

Calculation of Hill coefficient

The focus dose response curve was fitted to the Hill function with a constant additive term accounting for basal activity. The parameters were optimized using all methods of the “oWptimx()” function in the “optimx” R package, and the method with the best fit was selected[50]. The equation used was as follows:

bioRxiv preprint doi: https://doi.org/10.1101/2021.07.13.452147; this version posted July 13, 2021. The copyright holder for this preprint (which was not certified by peer review) is the author/funder. All rights reserved. No reuse allowed without permission.

$$a + \frac{k[NF\kappa B]^N}{Km^N + [NF\kappa B]^N},$$

where *N*, *Km, k,* and *a* represent the Hill coefficient (cooperativity), the binding affinity of NF-κB to the enhancer region, the rate constant for foci formation, and the constant additive term accounting for basal activity, respectively.

Clustering of Fano factor change

Hierarchical clustering of Fano factor changes across anti-IgM doses was performed using the "hclust()" function of R with the method option "ward.D2."

Quantitative RT-PCR (qRT-PCR) analysis

Total RNA was collected from the DT40 cells using a NucleoSpin RNA kit (Macherey-Nagel GmbH & Co.) and subjected to complementary DNA synthesis and quantitative PCR using a ReverTra Ace qPCR RT Kit and KOD SYBR qPCR kit (Toyobo Life Science) according to the manufacturer's protocol. PCR cycling conditions were as follows: 40 cycles of 10 s at 98°C, 10 s at 60°C, and 30 s at 68°C. The primers used for qRT-PCR are listed in Supplementary Table 3. Expression values (n = 3) were normalized to those of *GAPDH*.

Single-cell RNA-sequencing analysis

The DT40 cells were stimulated with anti-IgM (0, 0.01, 0.1, 1, and 10 μg/mL) for 1 h and sorted using an SH800 cell sorter (Sony) with a 130 μm sorting chip to select single cells. RamDA-seq with oligo-dT primer single-cell RNA-seq method was used for cDNA preparation[33]. The samples were sequenced using HiSeq2500 (Illumina).

A quality check of the data was performed using FastQC. Trimming was performed using TrimGalore (with Cutadapt v2.3; https://www.bioinformatics.babraham.ac.uk/projects/trim_galore/) with default options, and alignment to the *Gallus gallus* reference genome (GRCg6a) was done using STAR v2.7.1a with default options[51]. Then, a gene count table was obtained from the alignment files using featureCounts v1.6.4 with "-t exon -g gene_id" options and the annotation GTF file GRCg6a.96 from ENSEMBL (ftp://ftp.ensembl.org/pub/release-96/gtf/gallus_gallus/)[52].

Seurat v3.2.1 was used for clustering and differential gene expression analysis of the scRNA-seq data[34]. Prior to clustering, a quality check of the data was performed to remove cell outliers (total count ≥ 1.5 million, detected genes ≥ 8500, and mitochondrial gene count ratio < 0.04) resulting in 89, 92, 87, 92, and 93 cells used in the analysis of the 0, 0.01, 0.1, 1, and 10 μg/mL anti-IgM concentrations, respectively. Data normalization was performed using Baynorm[53] and the log scaling method in Seurat. Data were regressed based on the cell cycle scoring with the "CellCycleScoring()" function of Seurat and mitochondrial gene count ratio. The top 2000 variable features were used for dimensionality reduction and clustering with a resolution of 0.2. Differentially expressed genes were extracted using the "FindAllMarkers()" function of Seurat. Pseudo-time analysis was performed by creating a principal curve using the Princurve v2.1.4 R package on the dimensionality-reduced projection with the Lowess smoother.

bioRxiv preprint doi: https://doi.org/10.1101/2021.07.13.452147; this version posted July 13, 2021. The copyright holder for this preprint (which was not certified by peer review) is the author/funder. All rights reserved. No reuse allowed without permission.

Single-cell ATAC-sequencing analysis

All protocols for generating scATAC-seq data on the 10x Chromium platform, including sample preparation, library preparation, and instrument and sequencing settings, are described below available here: https://support.10xgenomics.com/single-cell-atac. Prior to nuclei extraction, the DT40 cells were stimulated with 10 µg/mL of anti-IgM or PBS for 60 min.

Cellranger-atac count v1.1.0 (https://support.10xgenomics.com/single-cell-atac/software/pipelines/latest/algorithms/overview) was used with default options for performing quality checks and mapping the scATAC-seq data to the genome. The sequence files were downsampled to 250 million reads before running the Cellranger-atac count pipeline. The reference genome used was the ENSEMBL genome with the annotation file GRCg6a.96 (ftp://ftp.ensembl.org/pub/release-96/gtf/gallus_gallus/).

Identification of SEs and TEs

Peak calling and enhancer identification from ATAC-seq data were performed using Homer v4.10.4 (http://homer.ucsd.edu/homer/). A tag directory was created using the "makeTagDirectory" program with the "--sspe -single -tbp 1" option. Peak calling was performed using the "findPeaks" program with the "-style super -typical -minDist 5000 -L 0 -fdr 0.0001" option. Peak annotation was performed using the "annotatePeaks.pl" program with the GRCg6a.96 annotation file. Resulting peak files were merged between each stimulation condition for the SE and TE peaks using the "mergeBed" program of bedtools.

Gene ontology analysis

Gene ontology analysis was performed using the function "enrichGO" of clusterProfiler v3.14.3 for gained SE and RNA upregulated genes[54]. The Ensembl gene id was converted to the mouse homolog gene id prior to enrichment analysis.

Motif analysis

Motif score calculation for enhancer regions was performed using FIMO v5.0.5 with the database obtained from Homer v4.10.4[55]. The motif files from Homer were converted using the universalmotif v1.4.10 package of R.

Co-accessibility analysis

Peak calling was performed for co-accessibility analysis in Homer v4.10.4 using the "findPeaks" program with the "-style super -typical -minDist 0 -L 0 -fdr 0.0001" option to identify peaks constituting SE and TE. The "FeatureMatrix()" function of Signac v1.0.0 was used to assign fragments from the "fragments.tsv" file previously filtered for cell barcoding to the bed file containing peaks.

Cicero v1.3.4.10[28] was used to calculate the co-accessibility scores[28] between the ATAC peaks using the reference genome GRCg6a.96. The "max_sample_windows" argument of the "distance_parameters()" function was set to 1000, and the "max_elements" argument of the "generate_cicero_models()" function was set to 500. The other options were set to default. Co-accessibility calculations were performed separately for both the stimulated and unstimulated cells. The final co-accessibility scores were determined as the differences between the co-accessibility scores of the

bioRxiv preprint doi: https://doi.org/10.1101/2021.07.13.452147; this version posted July 13, 2021. The copyright holder for this preprint (which was not certified by peer review) is the author/funder. All rights reserved. No reuse allowed without permission.

stimulated cells and unstimulated cells, where the initial score ≥ 0.1 in the stimulated cells. Gviz v1.30.3 was used to visualize the co-accessibility between genomic regions.

mKate2-BRD4S transposon plasmid construction

We engineered the PB-TA-ERP2-mKate2-BRD4S construct from two addgene clones (65378[56] and 80477[57]) and pmKate2-H2B (Evrogen). Overlap extension PCR was performed to amplify the mKate2 insert from the mKate2-H2B plasmid while adding the attB1 adapter and linker sequence. Another round of overlap extension PCR was performed to amplify the BRD4S insert from GFP-BRD4 while adding the attB2 adapter and linker sequence. A final round of fusion PCR was performed to fuse the fragments containing mKate2 and BRD4 to create an insert containing mKate2-linker-BRD4S. The primers used for the overlap extension PCR are listed in Supplementary Table 4. A BP reaction using BP Clonase II (Invitrogen) was performed to clone the insert into pDONR221 (Invitrogen), creating the entry clone pENTR221-mKate2-BRD4S. The entry clone was amplified using NEB-Stable (New England Biolabs). An LR reaction using LR Clonase II (Invitrogen) was performed with the destination vector PB-TA-ERP2[57] to create the final expression vector.

Cell transfection

Cell transfection was performed using the Neon Transfection System (Invitrogen). A total of 2 μg of tplasmid was mixed with 1×10^6 cells in 10 μL buffer R. Electroporation was performed at 1400 V for 30 ms with 1 pulse. For piggyBac co-transfection, a mass ratio of 1:3 (PB:pBase) of the plasmid was used.

Statistics and reproducibility

The qPCR data are presented as the mean ± standard deviation (SD), wherein N = number of biological replicates. Data were evaluated using the unpaired Student's t-test for statistical significance. The means were considered statistically significant at $p < 0.05$. Box plots represent the median (center line), interquartile range (IQR; box limits), and 1.5× IQR for the whiskers.

Data availability

All sequencing data were deposited in the DNA Data Bank of Japan (DDBJ) under the accession number DRA012330. The codes used for the bioinformatics analysis and imaging analysis are available at https://github.com/okadalabipr/Wibisana2021. Other data are available from the corresponding author upon request.

Acknowledgements

We thank Dr. Kazuo Yamashita and Dr. Masakazu Ishikawa of KOTAI Biotechnologies, Inc. (Suita, Osaka) for preparing the scATAC-seq samples. We thank Dr. Akira Imamoto and Dr. Shinpei Kawaoka for their discussions regarding plasmid

bioRxiv preprint doi: https://doi.org/10.1101/2021.07.13.452147; this version posted July 13, 2021. The copyright holder for this preprint (which was not certified by peer review) is the author/funder. All rights reserved. No reuse allowed without permission.

construction and CRISPR-Cas9 experiments as well as Dr. Takeya Kasukawa for discussion regarding NGS analysis. M.O. was supported by JSPS KAKENHI grants 17H06299, 17H06302, and 18H04031 as well as JST-Mirai Program grant JPMJMI19G7. Y.S was supported by JSPS KAKENHI grant 19K22404. I. N. was partially supported by JST CREST grant JPMJCR16G3 and JPMJCR1926. This research was partially supported by the Platform Project for Supporting in Drug Discovery and Life Science Research (Platform for Drug Discovery, Informatics, and Structural Life Science) from the Japan Agency for Medical Research and Development (AMED). J. N. W. was supported by the Honjo International Scholarship Foundation.

Author contributions

J.N.W. performed computational data analysis of the scRNA-seq and scATAC-seq, smFISH experiments and constructed the BRD4S-mKate2 cells. J.N.W., T.I., and Y.S. performed the imaging analyses. H.S. and N. Y. constructed the RelA-GFP-expressing cells and prepared the samples for scRNA-seq. T. H., M. U., M. E., and I. N. performed the single-cell sorting and RamDA-seq. J.N.W., T. I., Y. S., and M.O. interpreted the analysis results. J.N.W. and M.O. wrote the manuscript. Y.S. and M.O. conceived the study and performed overall direction and planning.

Competing interests

The authors declare no competing interests.

bioRxiv preprint doi: https://doi.org/10.1101/2021.07.13.452147; this version posted July 13, 2021. The copyright holder for this preprint (which was not certified by peer review) is the author/funder. All rights reserved. No reuse allowed without permission.

References

1. Stanic, A. K. *et al.* NF-κB Controls Cell Fate Specification, Survival, and Molecular Differentiation of Immunoregulatory Natural T Lymphocytes. *J. Immunol.* **172**, 2265–2273 (2004).

2. Hayden, M. S. & Ghosh, S. NF-κB, the first quarter-century: Remarkable progress and outstanding questions. *Genes Dev.* **26**, 203–234 (2012).

3. Basak, S., Behar, M. & Hoffmann, A. Lessons from mathematically modeling the NF-κB pathway. *Immunol. Rev.* **246**, 221–238 (2012).

4. Kurosaki, T. Regulation of B cell fates by BCR signaling components. *Curr. Opin. Immunol.* **14**, 341–347 (2002).

5. Schulze-Luehrmann, J. & Ghosh, S. Antigen-Receptor Signaling to Nuclear Factor κB. *Immunity* **25**, 701–715 (2006).

6. Bonizzi, G. & Karin, M. The two NF-κB activation pathways and their role in innate and adaptive immunity. *Trends Immunol.* **25**, 280–288 (2004).

7. Shinohara, H. *et al.* Positive feedback within a kinase signaling complex functions as a switch mechanism for NF-κB activation. *Science* **344**, 760–4 (2014).

8. Michida, H. *et al.* The Number of Transcription Factors at an Enhancer Determines Switch-like Gene Expression. *Cell Rep.* **31**, 107724 (2020).

9. Mitchell, S., Roy, K., Zangle, T. A. & Hoffmann, A. Nongenetic origins of cell-to-cell variability in B lymphocyte proliferation. *Proc. Natl. Acad. Sci.* **115**, E2888–E2897 (2018).

10. Roy, K. *et al.* A Regulatory Circuit Controlling the Dynamics of NF-κB cRel Transitions B Cells from Proliferation to Plasma Cell Differentiation. *Immunity* **50**, 616-628.e6 (2019).

11. Paszek, P. *et al.* Population robustness arising from cellular heterogeneity. *Proc. Natl. Acad. Sci. U. S. A.* **107**, 11644–11649 (2010).

12. Tay, S. *et al.* Single-cell NF-κB dynamics reveal digital activation and analogue information processing. *Nature* **466**, 267–271 (2010).

13. Whyte, W. A. *et al.* Master transcription factors and mediator establish super-enhancers at key cell identity genes. *Cell* **153**, 307–319 (2013).

14. Hnisz, D. *et al.* Super-enhancers in the control of cell identity and disease. *Cell* **155**, 934 (2013).

15. Brown, J. D. *et al.* NF-κB directs dynamic super enhancer formation in inflammation and atherogenesis. *Mol. Cell* **56**, 219–231 (2014).

16. Zou, Z. *et al.* Brd4 maintains constitutively active NF-κB in cancer cells by binding to acetylated RelA. *Oncogene* **33**, 2395–2404 (2014).

17. Sabari, B. R. *et al.* Coactivator condensation at super-enhancers links phase separation and gene control. *Science (80-.).* **361**, eaar3958 (2018).

18. Schneider, N. *et al.* Liquid-liquid phase separation of light-inducible

bioRxiv preprint doi: https://doi.org/10.1101/2021.07.13.452147; this version posted July 13, 2021. The copyright holder for this preprint (which was not certified by peer review) is the author/funder. All rights reserved. No reuse allowed without permission.

transcription factors increases transcription activation in mammalian cells and mice. *Sci. Adv.* **7**, (2021).

19. Shrinivas, K. *et al.* Enhancer Features that Drive Formation of Transcriptional Condensates. *Mol. Cell* **75**, 549-561.e7 (2019).

20. Boija, A. *et al.* Transcription Factors Activate Genes through the Phase-Separation Capacity of Their Activation Domains. *Cell* **175**, 1842-1855.e16 (2018).

21. Faure, A. J., Schmiedel, J. M. & Lehner, B. Systematic Analysis of the Determinants of Gene Expression Noise in Embryonic Stem Cells. *Cell Syst.* **5**, 471-484.e4 (2017).

22. Hnisz, D., Shrinivas, K., Young, R. A., Chakraborty, A. K. & Sharp, P. A. A Phase Separation Model for Transcriptional Control. *Cell* **169**, 13–23 (2017).

23. Sun, S. C., Ganchi, P. A., Ballard, D. W. & Greene, W. C. NF-κB controls expression of inhibitor IκBα: Evidence for an inducible autoregulatory pathway. *Science (80-.).* **259**, 1912–1915 (1993).

24. McKinsey, T. A., Chu, Z. L., Tedder, T. F. & Ballard, D. W. Transcription factor NF-κB regulates inducible CD83 gene expression in activated T lymphocytes. *Mol. Immunol.* **37**, 783–788 (2000).

25. Zhao, M. *et al. Transcriptional outcomes and kinetic patterning of gene expression in response to NF-κB activation*. *PLoS Biology* **16**, (2018).

26. Brown, K., Park, S., Kanno, T., Franzoso, G. & Siebenlist, U. Mutual regulation of the transcriptional activator NF-κB and its inhibitor, IκB-α. *Proc. Natl. Acad. Sci. U. S. A.* **90**, 2532–2536 (1993).

27. Krzyzak, L. *et al.* CD83 Modulates B Cell Activation and Germinal Center Responses. *J. Immunol.* **196**, 3581–3594 (2016).

28. Pliner, H. A. *et al.* Cicero Predicts cis-Regulatory DNA Interactions from Single-Cell Chromatin Accessibility Data. *Mol. Cell* **71**, 858-871.e8 (2018).

29. Pott, S. & Lieb, J. D. What are super-enhancers? *Nat. Genet.* **47**, 8–12 (2015).

30. Romero, P. *et al.* Sequence complexity of disordered protein. *Proteins Struct. Funct. Genet.* **42**, 38–48 (2001).

31. Dunker, A. K., Brown, C. J., Lawson, J. D., Iakoucheva, L. M. & Obradović, Z. Intrinsic disorder and protein function. *Biochemistry* **41**, 6573–6582 (2002).

32. Alberti, S., Gladfelter, A. & Mittag, T. Considerations and Challenges in Studying Liquid-Liquid Phase Separation and Biomolecular Condensates. *Cell* **176**, 419–434 (2019).

33. Hayashi, T. *et al.* Single-cell full-length total RNA sequencing uncovers dynamics of recursive splicing and enhancer RNAs. *Nat. Commun.* **9**, (2018).

34. Butler, A., Hoffman, P., Smibert, P., Papalexi, E. & Satija, R. Integrating single-cell transcriptomic data across different conditions, technologies, and species. *Nat. Biotechnol.* **36**, 411–420 (2018).

bioRxiv preprint doi: https://doi.org/10.1101/2021.07.13.452147; this version posted July 13, 2021. The copyright holder for this preprint (which was not certified by peer review) is the author/funder. All rights reserved. No reuse allowed without permission.

35. Krikos, A., Laherty, C. D. & Dixit, V. M. Transcriptional activation of the tumor necrosis factor α-inducible zinc finger protein, A20, is mediated by κB elements. *J. Biol. Chem.* **267**, 17971–17976 (1992).

36. Munsky, B., Neuert, G. & Van Oudenaarden, A. Using gene expression noise to understand gene regulation. *Science (80-.).* **336**, 183–187 (2012).

37. Hansen, M. M. K., Desai, R. V., Simpson, M. L. & Weinberger, L. S. Cytoplasmic Amplification of Transcriptional Noise Generates Substantial Cell-to-Cell Variability. *Cell Syst.* **7**, 384-397.e6 (2018).

38. Shembade, N. & Harhaj, E. W. Regulation of NF-κB signaling by the A20 deubiquitinase. *Cell. Mol. Immunol.* **9**, 123–130 (2012).

39. Bass, V. L., Wong, V. C., Bullock, M. E., Gaudet, S. & Miller-Jensen, K. TNF stimulation primarily modulates transcriptional burst size of NF-κB-regulated genes. *bioRxiv* 2020.11.16.384297 (2020). doi:10.1101/2020.11.16.384297

40. Yan, F., Powell, D. R., Curtis, D. J. & Wong, N. C. From reads to insight: A hitchhiker's guide to ATAC-seq data analysis. *Genome Biol.* **21**, 1–16 (2020).

41. Lovén, J. *et al.* Selective inhibition of tumor oncogenes by disruption of super-enhancers. *Cell* **153**, 320–334 (2013).

42. Dukler, N., Gulko, B., Huang, Y. F. & Siepel, A. Is a super-enhancer greater than the sum of its parts? *Nat. Genet.* **49**, 2–4 (2017).

43. Zamudio, A. V. *et al.* Mediator Condensates Localize Signaling Factors to Key Cell Identity Genes. *Mol. Cell* **76**, 753-766.e6 (2019).

44. Ochab-Marcinek, A. & Tabaka, M. Bimodal gene expression in noncooperative regulatory systems. *Proc. Natl. Acad. Sci. U. S. A.* **107**, 22096–22101 (2010).

45. Xue, Q. *et al.* Analysis of single-cell cytokine secretion reveals a role for paracrine signaling in coordinating macrophage responses to TLR4 stimulation. *Sci. Signal.* **8**, ra59 (2015).

46. Shalek, A. K. *et al.* Single-cell RNA-seq reveals dynamic paracrine control of cellular variation. *Nature* **510**, 363–369 (2014).

47. Huang, J. *et al.* Dissecting super-enhancer hierarchy based on chromatin interactions. *Nat. Commun.* **9**, (2018).

48. Bothma, J. P. *et al.* Enhancer additivity and non-additivity are determined by enhancer strength in the Drosophila embryo. *Elife* **4**, 1–14 (2015).

49. Mueller, F. *et al.* FISH-quant: Automatic counting of transcripts in 3D FISH images. *Nat. Methods* **10**, 277–278 (2013).

50. Nash, J. C. & Varadhan, R. Unifying Optimization Algorithms to Aid Software System Users: optimx for R. *J. Stat. Softw.* **43**, (2011).

51. Dobin, A. *et al.* STAR: ultrafast universal RNA-seq aligner. *Bioinformatics* **29**, 15–21 (2013).

52. Liao, Y., Smyth, G. K. & Shi, W. featureCounts: an efficient general purpose program for assigning sequence reads to genomic features. *Bioinformatics* **30**,

bioRxiv preprint doi: https://doi.org/10.1101/2021.07.13.452147; this version posted July 13, 2021. The copyright holder for this preprint (which was not certified by peer review) is the author/funder. All rights reserved. No reuse allowed without permission.

923–930 (2014).

53. Tang, W. *et al.* bayNorm: Bayesian gene expression recovery, imputation and normalization for single-cell RNA-sequencing data. *Bioinformatics* **36**, 1174–1181 (2019).

54. Yu, G., Wang, L. G., Han, Y. & He, Q. Y. ClusterProfiler: An R package for comparing biological themes among gene clusters. *Omi. A J. Integr. Biol.* **16**, 284–287 (2012).

55. Grant, C. E., Bailey, T. L. & Noble, W. S. FIMO: scanning for occurrences of a given motif. *Bioinformatics* **27**, 1017–1018 (2011).

56. Gong, F. *et al.* Screen identifies bromodomain protein ZMYND8 in chromatin recognition of transcription-associated DNA damage that promotes homologous recombination. *Genes Dev.* **29**, 197–211 (2015).

57. Kim, S. Il *et al.* Inducible transgene expression in human iPS cells using versatile all-in-one piggybac transposons. *Methods Mol. Biol.* **1357**, 111–131 (2016).

bioRxiv preprint doi: https://doi.org/10.1101/2021.07.13.452147; this version posted July 13, 2021. The copyright holder for this preprint (which was not certified by peer review) is the author/funder. All rights reserved. No reuse allowed without permission.

Figures

Figure 1

RelA foci demonstrate SE-like properties.

(a) Representative real-time fluorescence micrographs of an individual RelA-GFP-expressing DT40 cell upon stimulation with 10 μg/mL anti-IgM (scale bar, 25 μm) and the quantification of the number of foci per cell across various anti-IgM doses (red points represent the median). (b) Quantification of the number of foci per cell after 20 min of various doses of anti-IgM stimulation (red dots represent the median). The median value was fitted to the Hill equation, resulting in a Hill coefficient of 4.33. (c) Time-lapse fluorescence micrograph of DT40 cells co-expressing mKate2-BRD4S and RelA-GFP upon stimulation with 10 μg/mL anti-IgM (scale bar, 5 μm). (d) Quantification of the co-localization of mKate2-BRD4S and RelA-GFP 20 min after anti-IgM stimulation. (e) Representative fluorescence micrographs of RelA-GFP-expressing DT40 cells pre-treated with 5 μM JQ1 for 60 min or 4 μM IKK-16 for 60 min. (f) Quantification of RelA foci from (e). (g) Quantification of RelA-GFP foci before treatment, after 1,6-hexanediol treatment, and after washing. The threshold of foci detection was lowered to compensate for the low fluorescence intensities of the recovering foci.

Figure 2

NF-κB SE-regulated genes demonstrate SE-like dynamics.

(a) UMAP projection of the dimensionality reduction and clustering results of approximately 450 cells scRNA-seq stimulated with various anti-IgM doses. (b) Box plot of the expression of known marker genes used to identify activated (red) and inactivated (blue) cell clusters. (c) Cell activation ratio from imaging obtained using logistic regression of foci at 20 min compared with the cell activation ratio from RNA-seq. (d) Hierarchical clustering analysis of Fano factors across anti-IgM concentrations for marker genes. The red lines represent the means. (e) Single-cell expression of *CD83* (B cell activation marker) and *NFKBIA* (NF-κB target gene) obtained from scRNA-seq across pseudo-time. (f) Micrograph of *CD83* and *NFKBIA* smRNA-FISH (scale bar, 5 μm). (g) Single-cell expression of *CD83* and *NFKBIA* obtained from scRNA-seq and smRNA-FISH after stimulation with 10 and 0 μg/mL anti-IgM.

Figure 3

SE analysis of *NFKBIA* and *CD83*.

(a) Plot of SEs determined using the ROSE algorithm[13] from cells with and without anti-IgM stimulation. (b) Scatter plot of SE-associated genes with significantly upregulated and downregulated mRNA levels in activated cells. (c) Scatter plot of DEG expression comparisons between inactivated and activated cells against SE and TE fold changes. (d) Time-course RT-qPCR of *CD83* and *NFKBIA* upon stimulation with 1 μg/mL anti-IgM. Gene expression was normalized to *GAPDH*. Error bar = SD. (e–f) RT-qPCR results after (e) IKK-16 and (f) JQ1 treatment 60 min prior to stimulation with 1 μg/mL anti-IgM for 60 min (N = 3). Gene expression was normalized to *GAPDH,* and

bioRxiv preprint doi: https://doi.org/10.1101/2021.07.13.452147; this version posted July 13, 2021. The copyright holder for this preprint (which was not certified by peer review) is the author/funder. All rights reserved. No reuse allowed without permission.

P-values were calculated using Student's unpaired t-test against dose 0 for each dose point. Error bar = SD.

Figure 4

Prediction of cis-regulatory regulation correlates with transcriptional noise.

(a) Correlation plot of Fano factor ratios (10 vs 0 μg/mL anti-IgM-stimulated cells) against intensity fold changes at SEs and TEs of marker genes. R = spearman correlation. (b) Correlation plot of RNA fold changes (activated vs inactivated cells) against numbers of co-accessible pairs. R = spearman correlation. (c) Correlation plot of Fano factor ratios (10 vs 0 μg/mL anti-IgM-stimulated cells) against numbers of co-accessible pairs. R = spearman correlation. (d–e) Co-accessibility score differences obtained using Cicero between stimulated and unstimulated cells shown between genomic regions interacting with regions ±1 kb around the annotated start site of *CD83*. The red arrows indicate regions that do not intersect with gene body of *CD83* or other genes.

bioRxiv preprint doi: https://doi.org/10.1101/2021.07.13.452147; this version posted July 13, 2021. The copyright holder for this preprint (which was not certified by peer review) is the author/funder. All rights reserved. No reuse allowed without permission.

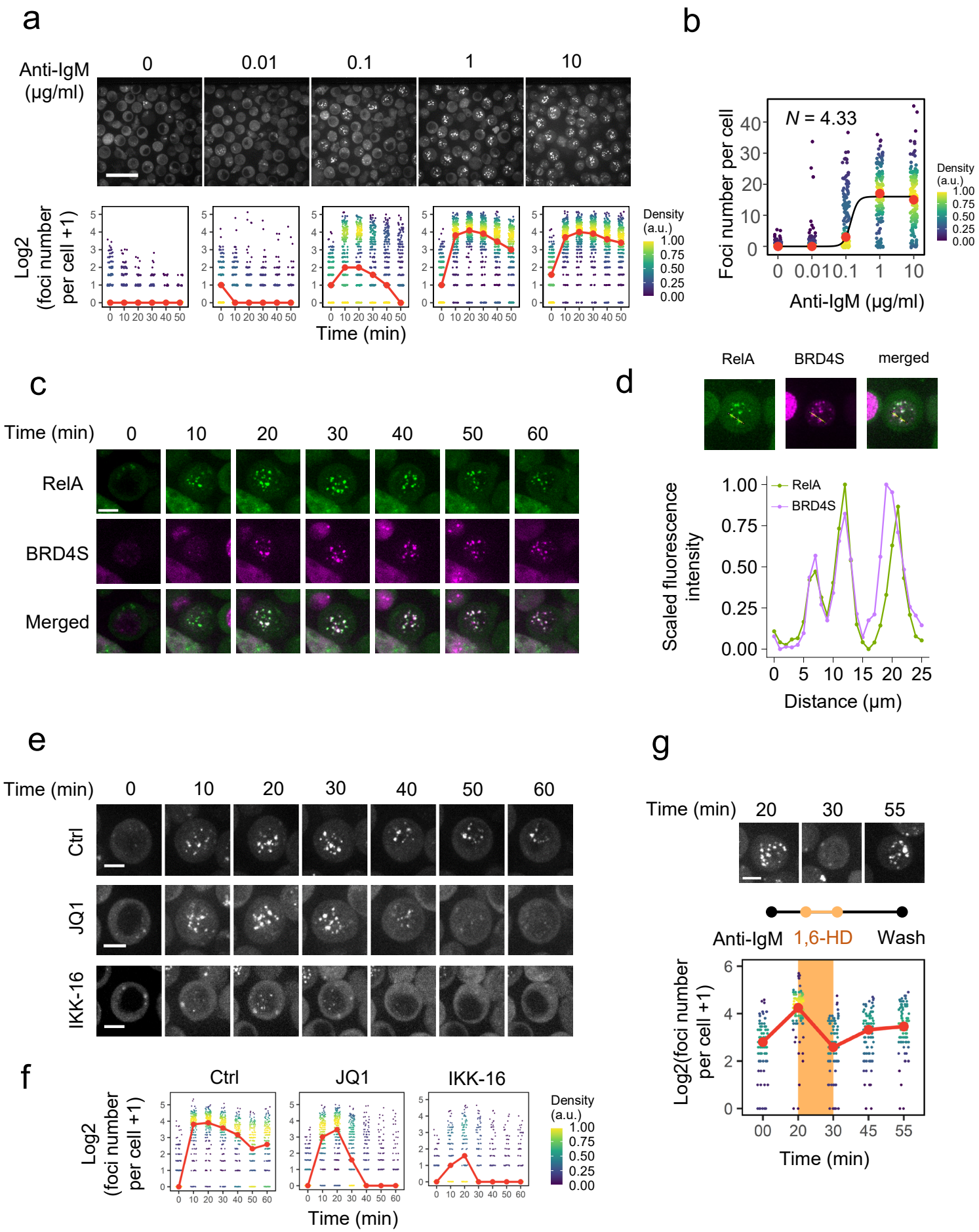

Fig 1

bioRxiv preprint doi: https://doi.org/10.1101/2021.07.13.452147; this version posted July 13, 2021. The copyright holder for this preprint (which was not certified by peer review) is the author/funder. All rights reserved. No reuse allowed without permission.

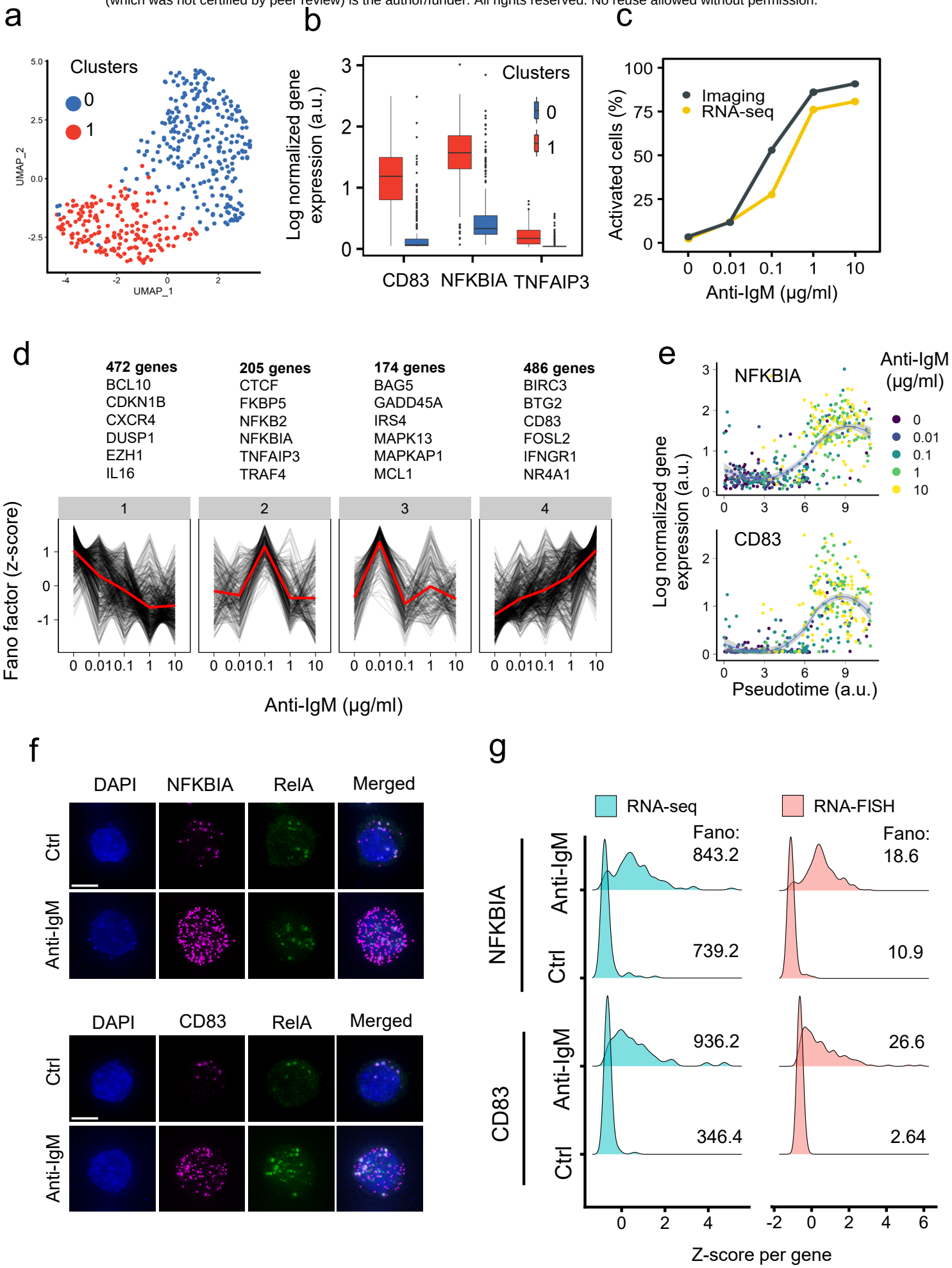

Fig 2

bioRxiv preprint doi: https://doi.org/10.1101/2021.07.13.452147; this version posted July 13, 2021. The copyright holder for this preprint (which was not certified by peer review) is the author/funder. All rights reserved. No reuse allowed without permission.

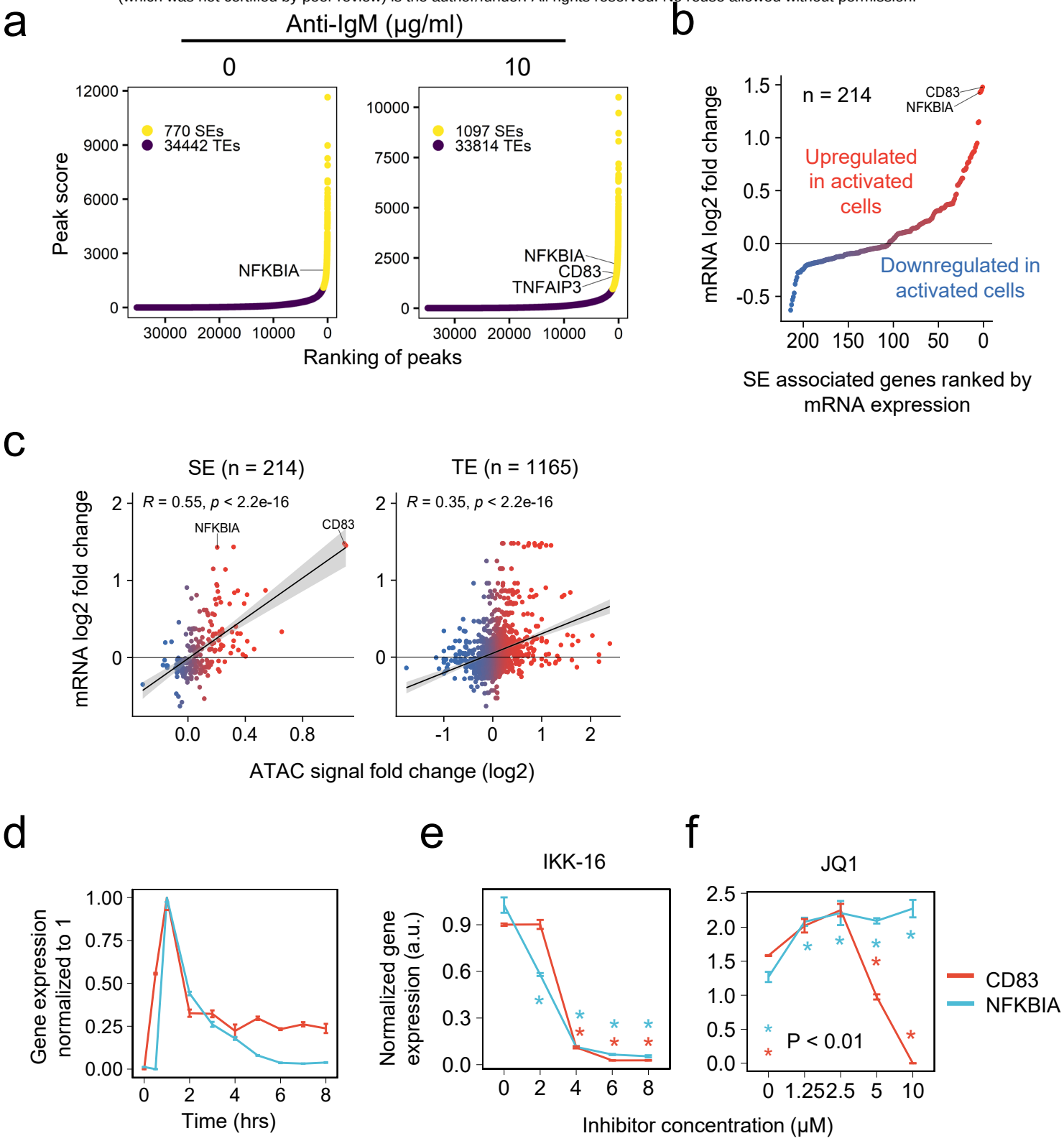

Fig 3

bioRxiv preprint doi: https://doi.org/10.1101/2021.07.13.452147; this version posted July 13, 2021. The copyright holder for this preprint (which was not certified by peer review) is the author/funder. All rights reserved. No reuse allowed without permission.

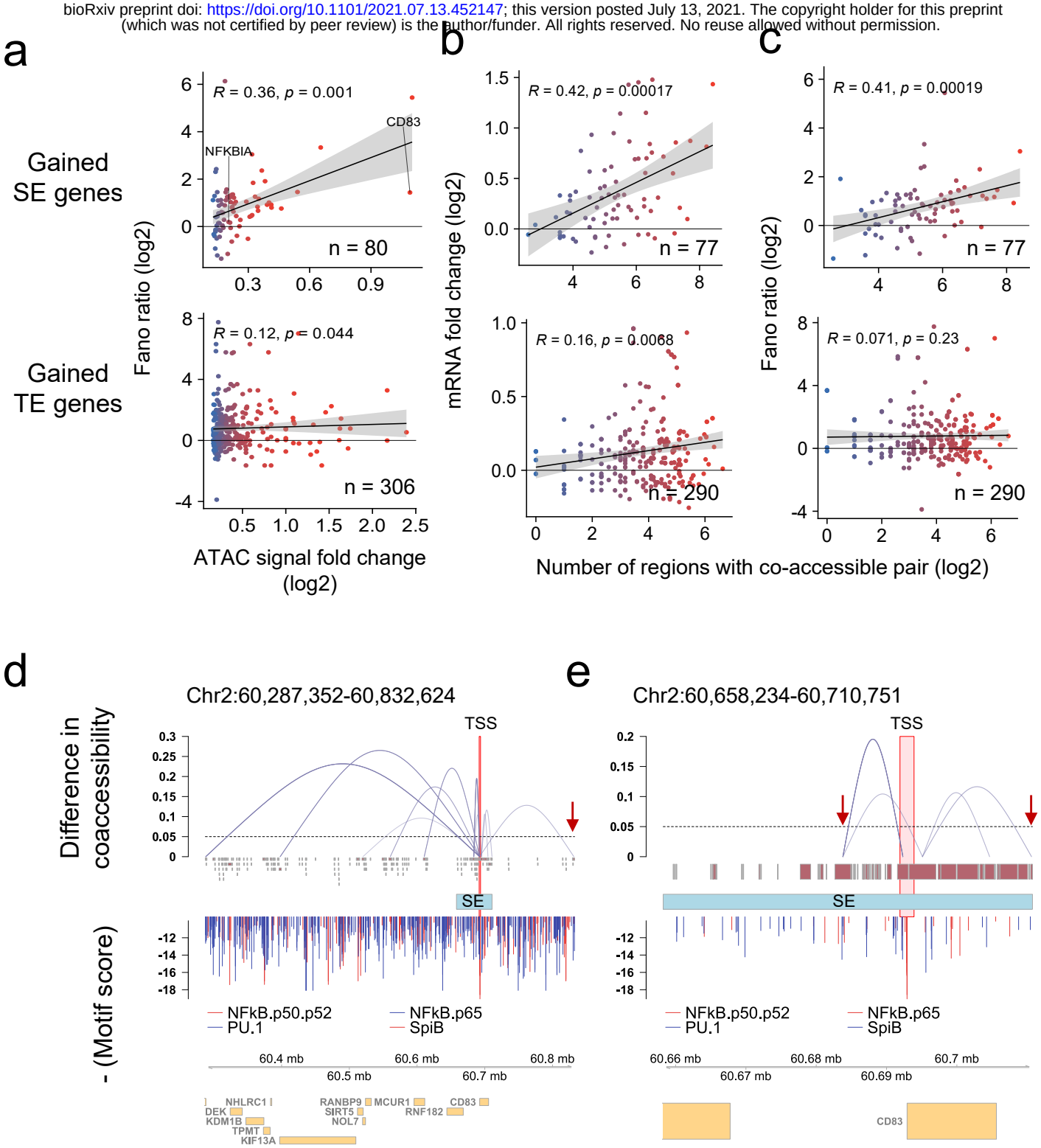

Fig 4